Generalized Swing Control Framework for Inverter-based Resources

Rodrigo Bernal and Federico Milano School of Electrical & Electronic Engineering, University College Dublin, Ireland rodrigo.bernal@ucdconnect.ie, federico.milano@ucd.ie

Abstract—This paper proposes a novel control framework designed for Inverter-Based Resources (IBRs), denoted as Generalized Swing Control (GSC). The proposed GSC framework generalizes the definition of Grid-Forming (GFM) control schemes and exploits the coupling between active and reactive power dynamics. To validate the proposed scheme, we conduct extensive time-domain simulations and small-signal analysis using a modified version of the WSCC 9-bus system and a 1479-bus dynamic model of the all-island Irish transmission system. The case studies focus on evaluating the dynamic performance of the proposed framework under different configurations, including Virtual Synchronous Machine (VSM), coupled-VSM and dual-VSM schemes. To address the nonlinear nature of power system dynamics, sensitivity analysis based on Monte Carlo methods are employed to improve parameter tuning and assess the stability of GSC configurations in the studied systems.

Index Terms—Low-inertia power systems, converter-interfaced generation, frequency control, swing equation, voltage control.

I. Introduction

A. Motivation

A fundamental difference between Inverter-Based Resources (IBRs) and conventional Synchronous Machines (SMs) is that the dynamic response of SMs is determined by their electromechanical dynamics, whereas that of IBRs is governed by their control schemes. This feature makes IBRs highly flexible and enables the design of a wide range of control schemes with diverse objectives [1]. Motivated by the dynamics of SMs and with the aim of defining a flexible general control of IBRs, this paper explores the extension of the SM swing equation into the complex power domain.

B. Literature Review

In grids characterized by high R/X ratios or with high penetration of IBRs, the conventional paradigm of decoupled active power/frequency and reactive power/voltage is not always true. Reference [2] shows that voltage/frequency stability is impacted by both self- and coupled-dynamics. Moreover, voltage and frequency oscillate at the same frequency if the voltage-frequency coupled instability occurs. Recent analytical work has quantified this coupling and its implications for the fast frequency response of Battery Energy Storage Systemss (BESSs) in high-renewable grids [3], while new control strategies explicitly address such coupling effects [4], [5], [6], [7].

The limitations in flexibility of SMs and the challenges of weak grids have increased the adoption of GFM inverters.

This work is supported by Sustainable Energy Authority of Ireland (SEAI) by funding R. Bernal and F. Milano under project FRESLIPS, Grant No. RDD/00681.

These devices allow control-based energy conversion without relying on physical inertia. Several GFM control strategies have been proposed, including droop-based methods [8], [9], voltage oscillator control [10], and VSM among other schemes [11]. For the case of Grid-Following (GFL), [12] shows that there is a limit for this type of converters before the system becomes unstable, and this limit is strongly influenced by the type of grid support the converters provide and their proper tuning. Moreover, it has been demonstrated in [13], [14] that despite these challenges, GFL inverters can support even 100% inverter-based power systems.

Stability assessment tools of such modern systems are presented in [15], which include Lyapunov direct methods, the equal-area criterion, small-signal analysis, data-driven methods, and time-domain simulations, with the latter being the most widely used for highly nonlinear dynamics and the one used within this work. Even in a simple single-machine infinite-bus model, the transient behavior is more complicated than commonly thought [16]. Thus, advanced nonlinear control approaches have been proposed such as Lyapunov-based nonlinear control algorithm [17] and data-driven methods [18]. Moreover, to provide damping and inertia from IBRs, new system-level frameworks [19] and converter-level controls [20] have been developed.

In [21], a generalized swing equation for PLL-based IBRs is proposed, integrating angle and frequency dynamics into a unified control framework. In this vein, our work extends the swing equation into the complex domain, enabling simultaneous control of voltage and frequency dynamics. This formulation leverages the nonlinear power flexibility of IBRs and introduces an explicit coupling between active and reactive power with voltage magnitude and phase, offering new dynamic features and modeling flexibility.

C. Contributions

This paper proposes a novel control framework designed for IBRs, denoted as Generalized Swing Control (GSC). Leveraging IBR inherent flexibility, GSC extends SM energy conversion principles through a complex formulation. Furthermore, the GSC framework uses the concept of *coupled inertia, damping* and *stiffness*, which describe the direct coupling between active and reactive power dynamics. Additionally, we propose a performance index $\mu_{\rm ts}$ that captures the dynamic performance of relevant variables in transient conditions.

D. Paper Organization

The remainder of the paper is organized as follows. The proposed GSC is described in Section II. Case studies are

1

presented in Section III, where the features of a set of possible GSC configurations are studied. Finally, conclusions and future work are discussed in Section IV.

E. Notation

All variables are assumed to be time dependent unless explicitly stated. The symbol ' is used to refer to the time derivative. Complex vectors are denoted with \bar{u} , vectors with u, and matrices with u.

II. PROPOSED CONTROL

Let $x \in \mathbb{R}^2$ denote the generalized positions of a second order system defined by the following dynamics:

$$\mathbf{M}\mathbf{x}'' + \mathbf{D}(\mathbf{x}' - \mathbf{x}_o') + \mathbf{K}(\mathbf{x} - \mathbf{x}_o) = \mathbf{f}, \tag{1}$$

where M is known as the inertia matrix, D the damping matrix, K is the stiffness matrix, and f accounts for inputs [22]. By rewriting the system as a system of first order differential equations, and introducing 2 new state variables, we obtain the following structure:

$$\boldsymbol{\zeta}' = \begin{bmatrix} 0_{2\times2} & \mathbf{I}_{2\times2} \\ -\mathbf{M}^{-1}\mathbf{K} & -\mathbf{M}^{-1}\mathbf{D} \end{bmatrix} \boldsymbol{\zeta} - \begin{bmatrix} 0_{2\times1} \\ \boldsymbol{f} \end{bmatrix}$$
(2)

where $\zeta = \begin{bmatrix} x - x_o & x' - x'_o \end{bmatrix}^{\top}$. Let **A** be the matrix that multiplies ζ . Then, the eigenvalues $\bar{\lambda}$ of **A** satisfy the generalized eigenvalue problem:

$$\det(\bar{\lambda}^2 \mathbf{M} + \bar{\lambda} \mathbf{D} + \mathbf{K}) = \det(Q(\bar{\lambda})) = 0.$$
 (3)

The determinant can be turned into an ordinary polynomial, and its stability can be assessed accordingly, as follows:

$$\det(Q(\bar{\lambda})) = a_4 \bar{\lambda}^4 + a_3 \bar{\lambda}^3 + a_2 \bar{\lambda}^2 + a_1 \bar{\lambda} + a_0, \tag{4}$$

where the coefficients are:

$$\begin{split} &a_0 = \det(\mathbf{K})\,,\\ &a_1 = \operatorname{tr}(\operatorname{adj}\left(\mathbf{D}\mathbf{K}\right))\,,\\ &a_2 = \det(\mathbf{D}) + \operatorname{tr}(\operatorname{adj}\left(\mathbf{M}\mathbf{K}\right))\,,\\ &a_3 = \operatorname{tr}(\operatorname{adj}\left(\mathbf{M}\mathbf{D}\right))\,,\\ &a_4 = \det(\mathbf{M})\,. \end{split}$$

The formulation of (3) is in the form of Quadratic Eigenvalue Problem (QEP). We refer the interested reader to [22] for a discussion on this class of systems and a discussion of the properties of matrices M, D and K related to system stability.

In the context of the proposed IBR control scheme, the generalized position is the vector $\boldsymbol{u}_v = [\ln v, \theta_v]^\top$, where v and θ_v are the magnitude and phase angle, respectively, of the terminal bus voltage of the converter. Recalling the definition of complex frequency (see the Appendix), we observe that $\boldsymbol{\eta}_v = \boldsymbol{u}_v' = [\rho_v, \omega_v]^\top$ and, substituting into (1), we obtain the second order system:

$$\mathbf{M}\boldsymbol{\eta}_{v}^{\prime} + \mathbf{D}\left(\boldsymbol{\eta}_{v} - \boldsymbol{\eta}_{o}\right) + \mathbf{K}\left(\boldsymbol{u}_{v} - \boldsymbol{u}_{o}\right) = \boldsymbol{s} - \boldsymbol{s}_{o}. \tag{5}$$

where $s = [p, q]^{\top}$ represents the input power vector for the IBR, and u_o , η_o and s_o are set-point operating conditions.

Equation (5) describes the power balance of each converter with the grid. Then, the total energy of the IBR, which is provided by the energy sources and storage that are exchanged with the grid, is as follows:

$$\Delta E = \Re \left\{ \int_0^t (\mathbf{s} - \mathbf{s}_o) dt \right\}$$

$$= \Re \left\{ \int_0^t (\mathbf{M} \boldsymbol{\eta}_v' + \mathbf{D} (\boldsymbol{\eta}_v - \boldsymbol{\eta}_o) + \mathbf{K} (\boldsymbol{u}_v - \boldsymbol{u}_o)) dt \right\},$$
(6)

where ΔE refers to the variation in the exchanged energy,

$$\Re\left\{\int \mathbf{M}\boldsymbol{\eta}_v' dt\right\} = \int (M_{11}\rho_v' + M_{12}\omega_v') dt$$
$$= M_{11}\rho_v + M_{12}\omega_v + c_M$$

denotes the part of the exchanged energy that is provided by a virtual storage in variables ρ_v and ω_v ,

$$\Re \left\{ \int \mathbf{D} \left(\boldsymbol{\eta}_v - \boldsymbol{\eta}_o \right) dt \right\}$$

$$= \int \left(D_{11} (\rho_v - \rho_o) + D_{12} (\omega_v - \omega_o) \right) dt$$

$$= D_{11} \left(\int \frac{dv}{v} - \int \frac{dv_o}{v_o} \right) + D_{12} \int d(\theta - \theta_o)$$

$$= D_{11} \left(\ln v - \ln v_o \right) + D_{12} \left(\theta - \theta_o \right) + c_{\mathbf{D}}.$$

the part of the exchanged energy that is provided by a virtual damping in $\ln v$ and the phase angle, and

$$\Re \left\{ \int \mathbf{K} (\boldsymbol{u}_v - \boldsymbol{u}_o) dt \right\}$$

$$= \int (K_{11}(\ln v - \ln v_o) + K_{12}(\theta - \theta_o)) dt,$$

the part of the exchanged energy that is provided by the change in the potential energy. We note that the system is rheonomous, that is, the integral is explicitly time dependent, and it cannot be calculated without knowing the trajectory of the voltage magnitude and its phase.

Although in this work we define the control matrices as symmetric positive definite to satisfy theoretical properties, the practical implementation presents some challenges. The aggregation of multiple GSCs, combined with the inherent nonlinearities of power system networks, makes it difficult to track the full matrices of the full system QEP. As a consequence, extensive time-domain simulation analysis through Monte Carlo method are employed to improve the parameter tuning and assessment of the stability of GSC implementations in the studied systems.

A. Performance Metric

To evaluate the dynamic performance of the proposed control, the index $\mu_{ts,k}$ is used to quantify variations in voltage magnitude and phase at bus k taking into consideration transient and steady state. The index is defined as a weighted sum of quadratic errors in comparison to initial and final steady-state operation points as follows:

$$\mu_{\mathrm{ts},k} = \mu_{\mathrm{t},k} + \mu_{\mathrm{s},k},\tag{7}$$

where

$$\mu_{t,k} = \kappa_{t,\omega} \int (\omega_k - \omega_f)^2 dt + \kappa_{t,\rho} \int (\rho_k - \rho_f)^2 dt, \quad (8)$$

$$\mu_{s,k} = \kappa_{s,\omega} (\omega_{o} - \omega_{f})^{2} + \kappa_{s,v} (v_{o,k} - v_{f,k})^{2},$$
 (9)

where the sub-indexes t and s stand for transient and steadystate behavior, and o and f refer to the initial and final conditions. Thus, the parameters $\kappa_{s,\omega}$, $\kappa_{s,v}$, $\kappa_{t,\omega}$, $\kappa_{t,\rho}$ represent weights to assess the dynamic trajectory of the voltage phase and magnitude. These parameters can be adjusted according to the requirements of each system and the control objectives.

The proposed metric quantifies the quadratic error of each Complex Frequency (CF) component with respect to its final steady state, while including a weighted measure of the difference in voltage magnitude and frequency between initial and final conditions.

To assess the overall dynamic impact of all devices on the system, we define the index μ_{ts} as:

$$\mu_{\rm ts} = \mu_{\rm t} + \mu_{\rm s} = \sum_{i \in \mathcal{G}} (\mu_{{\rm t},i} + \mu_{{\rm s},i}),$$
(10)

where $\mathcal G$ represents the set of all buses in the grid in which a generator is connected. This index provides a scalar measure of the total voltage variation across the devices of the system. As $\mu_{\rm ts}$ is a cumulative metric, a smaller value indicates a more effective controller.

A similar performance index μ_k was defined in [5] based on the concept of the total variations of the voltage at a node. Nevertheless, the index in [5] is unable to capture steady-state performance.

III. CASE STUDIES

This section presents simulation results based on modified versions of the WSCC 9-bus system [23] and the all-island Irish transmission system described in [24]. In the first case, SMs are replaced by IBRs modeled using the proposed GSC framework, according to the details provided in Section II. For simplicity, all configuration settings are identical for all IBRs but are weighted by the generator base power. For the Irish system, the behaviors of the different GSC configurations are compared with the performance of an SM-based system.

For cases where power unbalance is applied, load variation is assumed to be a *sustained power perturbation*, namely, a step change of the grid power exchange that remains constant in the time scale of storage and control dynamics of the IBR.

To evaluate dynamic performance of the control, the index $\mu_{\rm ts}$ defined in Section II-A is used to quantify variations in the voltage magnitude and phase at the generator buses within the transient and in steady state.

We explore the impact on stability of the proposed GSC through a time-domain sensitivity analysis over the parameters of the GSC. This analysis is based on the Monte Carlo method, with a total of 20,000 realizations for each scenario. Each realization consists on eigenvalue calculations of the linearized system and time-domain simulations, varying the studied parameters within an explicit range. The sensitivity analysis for each parameter is used to calculate the performance metric $\mu_{\rm ts}$ and the unstable simulation rate. The latter is defined as

the ratio between the number of unstable simulations and the total number of simulations conducted for a specific parameter range. In particular, we assume that a simulation is stable if the following criteria are satisfied:

- 1) The real and imaginary parts of the complex frequency of the internal voltage of each IBRs converge to a steady-state value within a specified tolerance; that is, $\bar{\eta}_k = \rho_{\rm f} + \jmath \omega_{\rm f} + \bar{\epsilon}$, where $\bar{\epsilon}$ is a given tolerance.
- 2) The linearized system is asymptotically stable; that is, the real parts of the eigenvalues of the system are all negative: $\max(\Re{\{\bar{\lambda}\}}) < 0$.
- 3) All modes of the linearized system are slower than a threshold given by the minimum acceptable time constant T_{\min} . This is enforced by the following constraints:
 - The decay rate of each mode must be slower than the threshold T_{\min} ; particularly, the real parts must satisfy $-\Re\{\bar{\lambda}\} < T_{\min}^{-1}$.
 - The oscillation frequency of each mode must be slower than the threshold T_{\min} ; specifically, the imaginary parts must satisfy $|\Im\{\bar{\lambda}\}| < 2\pi \, T_{\min}^{-1}$

In this work, we adopt a tolerance $\bar{\epsilon}=10^{-10}(1+\jmath)$ and a minimum acceptable time constant $T_{\rm min}=0.01~{\rm s.}$ As a conservative assumption, modes faster than those defined through $T_{\rm min}$ are considered unstable, as they can lead to instabilities due to possible couplings with very fast dynamics that are not considered in the model.

For all IBRs, the parameters of the LC filters are as follows: $L_{\rm f}=0.2~{\rm mH}$, $R_{\rm f}=0~\Omega$ and $C_{\rm f}=0.265~\mu{\rm F}$. Additionally, all weights for the index $\mu_{\rm ts}$ are considered with unitary magnitude. All simulation results presented in this section were obtained using the simulation software tool Dome [25].

A. WSCC-9 bus system

For this case study, we explore several configurations of the GSC. We begin by analyzing the VSM and then extend it to a configuration with coupled power control by setting parameters such as K_{12} and M_{21} to non-zero values. We also study the dual case of the VSM, denoted as Dual Virtual Synchronous Machine (dVSM), originally proposed in [26], where active and reactive power are still decoupled. In this case, however, active power is linked to the real part of the CF of the voltage ρ_v , and the reactive power is linked to its imaginary part, ω_v . While other configurations are possible, we focus on this set of examples to highlight the main features of the proposed controller.

1) VSM configuration: The GSC framework allows to choose a specific combination of parameters that makes the controller behave similarly to a VSM. This is achieved by setting parameters M_{22} , D_{22} , D_{11} , and K_{11} non-null. M_{22} and D_{22} represent the virtual inertia and damping of the frequency, respectively; and D_{11} and K_{11} act as a first order voltage droop controller. With the rest of the parameters of the GSC set as null, active and reactive power balance is mostly coupled with frequency and voltage variations, respectively.

Monte Carlo time-domain simulations are conducted ranging parameters M_{22} , D_{22} , D_{11} , and K_{11} from 0.01 to 100. A uniform logarithmic distribution is utilized for all parameters.

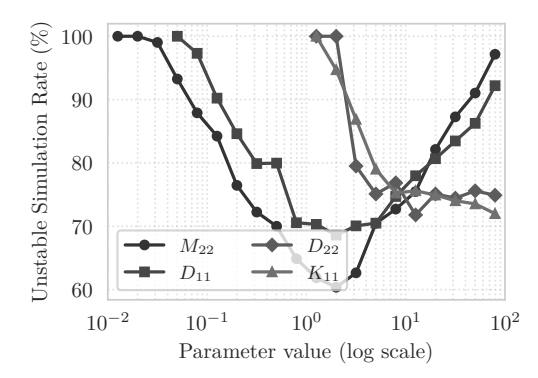


Fig. 1: WSCC 9-bus system - Sensitivity analysis based on the Monte Carlo method for VSM case - Unstable simulation rate as a function of parameter values in logarithm scale under a load variation at bus 5 applied at second 1 of the simulations

The contingency is a power unbalance given by a load variation of ± 0.5 pu in active and reactive power, where 0.5 pu corresponds to 15% of the total active power load and 40% of the reactive power load. The sign of the load variation is randomized, while the magnitude is kept invariant.

Figure 1 shows the unstable simulation rate in percentage for the WSCC 9-bus system and VSM configuration. The rate for each parameter ranges from 0.01 to 100 in logarithmic scale, and each point accounts for approximately 1000 simulations. The unstable simulation rate in Fig. 1 shows how each parameter impacts on the stability of the system. K_{11} stands for the stiffness in the variable $u_v = \ln v$, which has a similar effect on the stiffness in the voltage, and even more alike for voltages closer to the initial condition (u_0) . It is interesting to note that for values smaller than 1, all simulations are unstable. The same behavior is observed for D_{22} , which refers to the frequency damping controller. On the other hand, parameters such as M_{22} and D_{11} are not allowed to be too small, as they are directly related with the time constants, and neither too big, as they do not allow to reach a steady state within the specific time simulation period ($t_f = 20 \text{ s}$).

Figure 2 shows the metric $\mu_{\rm ts}$ as a function of the parameters M_{22} (panel a), D_{11} (panel b), D_{22} (panel c), and K_{11} (panel d) on a logarithmic scale. The top five configurations with the lowest metric values are highlighted in each panel. A direct relation between D_{22} and dynamic performance is observed, which is less evident for the other parameters.

This can be explained by the construction of the $\mu_{\rm ts}$ metric, as it measures both the difference between the initial and final steady-state frequencies (which is clearly reduced by increasing D_{22}) and the deviation of the frequency trajectory from its final steady-state value. The latter is minimized by a specific combination of parameters. For instance, an overdamped system may take too long to reach steady state, increasing the transient metric, while a small M_{22} can cause overshoot or oscillations, which also affects the metric.

2) Extended & Decoupled VSM configuration: In this subsection the role of the parameters M_{11} and K_{22} is assessed. Figure 3 illustrates the unstable simulation rate as a function of these parameters in logarithm scale under a load variation at bus 5 applied at second 1 of the simulations. Additionally,

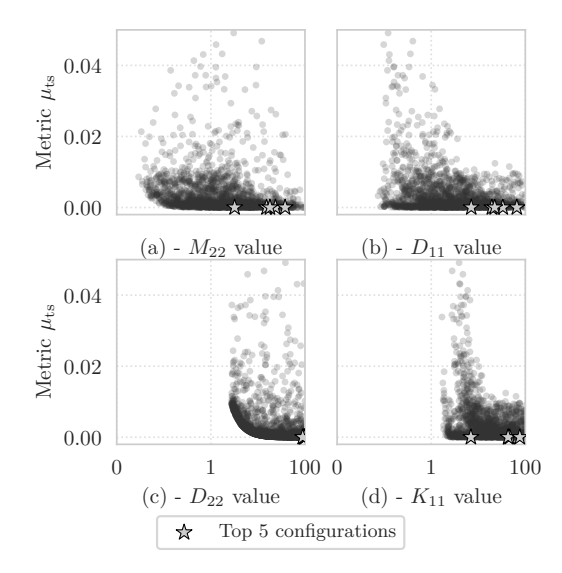


Fig. 2: WSCC 9-bus system - Sensitivity analysis based on the Monte Carlo method for VSM case - Performance metric $\mu_{\rm ts}$ as a function of parameter values in logarithm scale, M_{22} in panel (a), D_{11} , in panel (b), D_{22} in panel (c) and K_{11} in panel (d). Top 5 configurations are highlighted in each panel indicating the lowest metric values.

Fig. 4 displays the metric $\mu_{\rm ts}$ as a function of the parameters M_{11} (panel a) and K_{22} (panel b) on a logarithmic scale.

Figures 2 and 4 indicate that high values of K_{22} tend to marginally reduce the metric and increase the unstable simulation rate. Setting K_{22} to a non-null and positive value introduces integral control for the frequency. This can lead to several issues if not properly tuned, including unstable, unfair, or uneconomical active power distribution; windup problems; and poorly damped or even amplified oscillations.

The left panels of Fig. 5 illustrate the effect of K_{22} in the frequency and voltage at the terminals of the IBRs for three parameter values: 0, 0.01, and 0.1. The upper left panel shows how K_{22} mitigates frequency error and that higher gain values imply faster controller response, but at the cost of increased oscillatory behavior.

Parameter M_{11} acts as an inertia for the variable u_v , directly affecting the Rate of Change of Voltages (RoCoV). Although it does not have much influence in the metric for the studied range of the parameter as observed in Figure 4 (panel a), it has a significant effect on stability when increasing its value, as slower oscillatory responses do not reach a steady state in the simulation period. Finally, it is worth noting that voltage and frequency dynamics shown in Fig. 5 are not affected by K_{22} and M_{11} , respectively, which indicates that these variables are dynamically decoupled.

3) Coupled VSM configuration: In this subsection, a sensitivity analysis of the coupled terms in the active and reactive power balance is conducted. To achieve this, we start from the VSM and range terms such as D_{12} and D_{21} to couple the dynamic of the voltage magnitude with active power, and the dynamic of the voltage frequency to variations in reactive power. These parameters are varied equally ($D_{12} = D_{21}$). Thus, damping matrix \mathbf{D} is still symmetric. Symmetric damping matrices are often related to viscous damping, mutual impedance and proportional models, all of them of dissipative

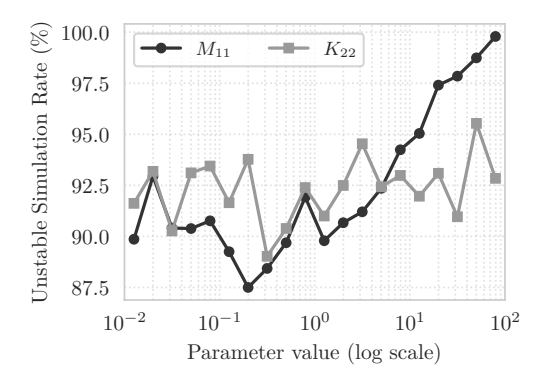


Fig. 3: WSCC 9-bus system - Sensitivity analysis based on the Monte Carlo method analysis for the extended VSM case - Unstable simulation rate as a function of parameter values in logarithm scale under a load variation at bus 5 applied at second 1 of the simulations.

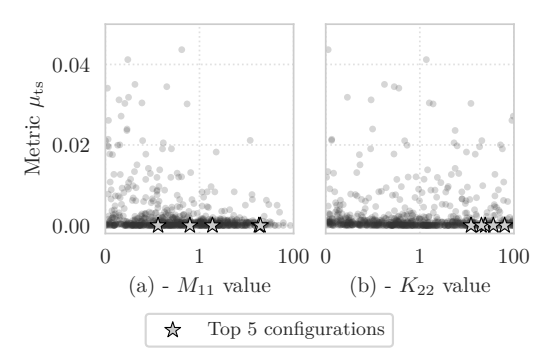


Fig. 4: WSCC 9-bus system - Sensitivity analysis based on the Monte Carlo method for the extended VSM case - Performance metric $\mu_{\rm ts}$ as a function of parameter values in logarithm scale, M_{11} in panel (a) and K_{22} in panel (b). Top 5 configurations are highlighted in each panel indicating the lowest metric values.

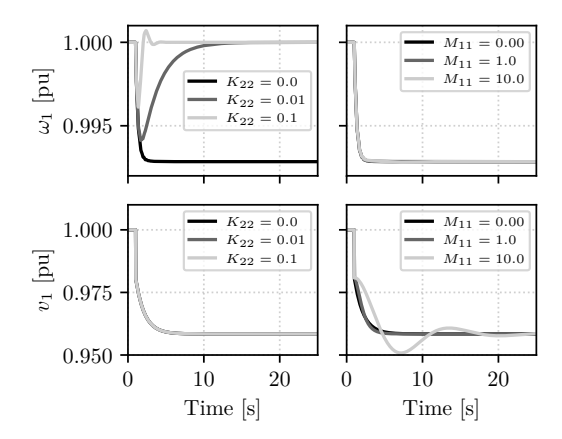


Fig. 5: WSCC 9-bus system - Extended & decoupled VSM analysis - Effect on frequency and magnitude of the voltage behavior at bus 1, for a variation in parameters K_{22} and M_{11} .

non-conservative nature. On the other hand, skew-symmetric damping matrices are often associated with gyroscopic terms and Coriolis effects, being both conservative phenomena.

Figure 6 shows the unstable simulation rate (panel a), and the value of the performance metric $\mu_{\rm ts}$ (panel b) as a function of parameter D_{12} ranging from 0.01 to 100. Top 5 configurations are highlighted.

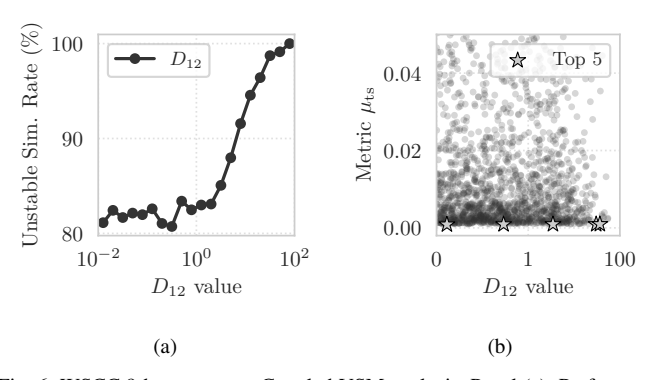


Fig. 6: WSCC 9-bus system – Coupled VSM analysis. Panel (a): Performance metric $\mu_{\rm ts}$ as a function of parameter D_{12} in logarithm scale. Panel (b): Unstable simulation rate as a function of D_{12} values in logarithm scale under a load variation at bus 5 applied at second 1 of the simulations. Top 5 configurations are highlighted.

In transmission systems the R/X ratio is relatively small, thus the inherent coupling between frequency and voltage with active and reactive power provided by the system becomes marginal. This effect can be observed in the performance metric presented in Figure 6-(b), where the change of value for parameters D_{12} and D_{21} don't have a significant effect on $\mu_{\rm ts}$. Nevertheless, increasing the value of the coupling parameter D_{12} increases the unstable simulation rate, as it introduces non wanted interactions of local voltage variations into the frequency dynamics, and vice-versa.

The effect of coupling parameters in the inertia and the stiffness matrix as well as the sensitivity in the R/X ratio is not studied in this paper and will be assessed in future work.

4) dVSM configuration: This subsection analyzes the dVSM configuration. In this setup, the elements of the power vector $s = [p,q]^{\top}$ on the right-hand side of (5) are interchanged, resulting in $\tilde{s} = [q,p]^{\top}$. The same transformation is applied to s_o .

For the dVSM configuration we set parameters M_{22} , D_{22} D_{11} and K_{11} non-zero. Thus, the dVSM voltage dynamics is linked with active power and frequency dynamics with reactive power. To address the main features of the dVSM, a sensitivity analysis based on the Monte Carlo method is conducted for these parameters, ranging them between 0.01 to 100.

Figure 7 illustrates the unstable simulation rate of the studied parameters. It is interesting to note that in general the rate is higher, suggesting a narrower number of stable combinations. Nevertheless, the shape of the rate as a function of the parameters is similar to the one displayed in Fig. 1 for the VSM configuration.

The performance metric assessment presented in Fig. 8 reveals a dual behavior among the studied parameters compared to the VSM case. This reflects that for the studied case, the active power balance has a major impact on the proposed

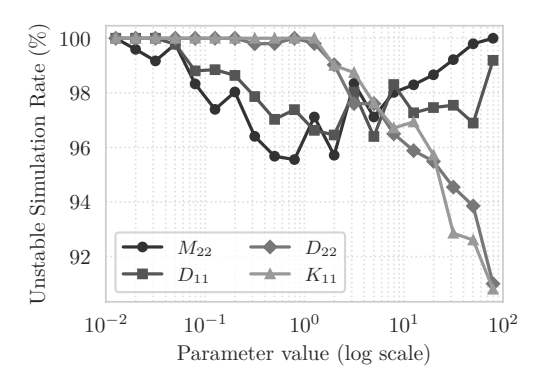


Fig. 7: WSCC 9-bus system - Sensitivity analysis based on the Monte Carlo method for dVSM case - Unstable simulation rate as a function of parameter values in logarithm scale.

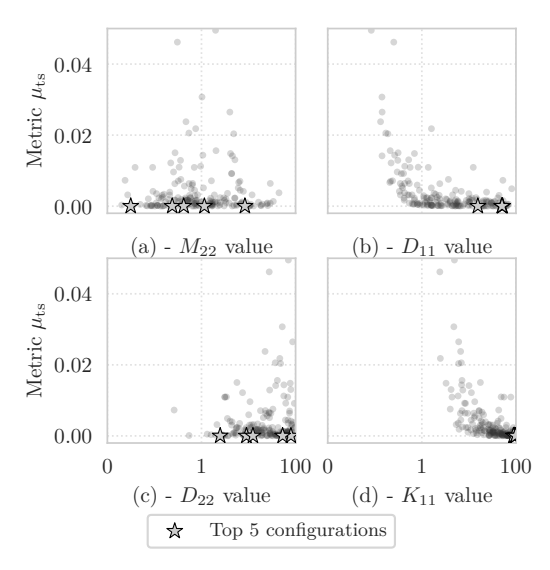


Fig. 8: WSCC 9-bus system - Sensitivity analysis based on the Monte Carlo method for dVSM case - Performance metric $\mu_{\rm ts}$ as a function of parameter values in logarithm scale, M_{11} in panel (a), M_{22} in panel (b), D_{11} in panel (c), D_{22} in panel (d), K_{11} in panel (e) and K_{22} in panel (f). Top 10 configurations are highlighted in each panel indicating the lowest metric values.

metric, while reactive power control acts as a supporting tool for stability. Furthermore, similar to the VSM configuration, the results prioritize faster controllers, provided they do not couple with other time scales.

B. Irish System

The grid comprises 21 synchronous generators, 169 wind plants, and 2 HVDC interconnectors. Additionally, there are 245 loads, 1479 buses, 796 lines, and 1055 transformers modeled within the system. Synchronous generators are modeled using Sauer and Pai's 6th order machine, simplified AVR IEEE type DC-1 with PSS2 and type 1 Turbine Governor, while wind turbines are modeled as Doubly-Fed Induction Generator (DFIG) (variable-speed 5th-order generator, double-mass elastic shaft with tower-shadow effect, turbine with continuous pitch control, cubic MPPT approximation, 1st-order AVR and turbine governor) and Constant Speed Induction Generator

(CSIG) (5th-order squirrel-cage induction generator model, turbine model without pitch control, single-mass shaft model with tower-shadow effect, and static capacitor bank) models. While simulations are based on realistic data, they do not represent any specific operational condition of the system.

Figure 9 shows the frequency of the center of inertia for the Irish grid, whereas Fig. 10 shows the voltage for various representative substations of the Irish grid located in the north, west, east and south of the system. The contingency consists in the loss of the East to West interconnector, which is importing its nominal active power of 500 MW. This is one of the most severe contingencies that can occur in the Irish transmission system in terms of power unbalance. In this scenario, we assume that the SMs and IBR have enough reserve to effectively provide the required active and reactive power lost during the event.

For the frequency of the Center of Inertia (CoI) calculation, we use the definition of virtual inertia adopted in [27] for systems with a significant share of IBRs, thus the frequency of the CoI is expressed as the following weighted sum:

$$\omega_{\text{CoI}} = \frac{\sum_{k \in \mathcal{K}_{\text{SM}}} H_k S_{b,k} \omega_k + \sum_{k \in \mathcal{K}_{\text{IBR}}} H_k S_{b,k} \omega_k}{\sum_{k \in \mathcal{K}_{\text{SM}}} H_k S_{b,k} + \sum_{k \in \mathcal{K}_{\text{IBR}}} H_k S_{b,k}}, \quad (11)$$

where H_k are the physical or virtual inertia time constants and $S_{b,k}$ are the capacities of the generators.

For the case when GSC is considered, all parameters for all devices are set equally. Thus, the inertia constants are simplified, and the frequency of the CoI becomes a weighted sum with respect to the base power of each device.

We compare the dynamic performance across four scenarios. The first is the base scenario without SM replacement. In the three remaining scenarios, SMs are replaced by IBRs with a GSC scheme configured as VSM; a VSM with coupling parameters $D_{12} = D_{21}$ (denoted as VSC-c); and finally, a dVSM scheme. Parameters of M, D and K are adjusted so that the initial Rate of Change of Frequency (RoCoF) and the steady-state value of the frequency and magnitude of the voltage are comparable. For the particular case of the dVSM we utilized the top values found in the Monte Carlo analysis within Section III-A4.

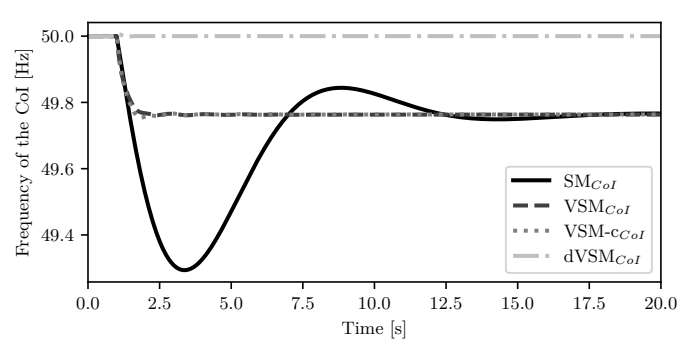


Fig. 9: Irish system - Frequency of the CoI after the loss of the East to West Interconnector 500 MW for different control setups of the GSC.

Although all scenarios satisfy the Irish grid technical requirements for frequency and voltage during transient system disturbances ([48, 52] Hz and [200, 245] kV for 220 kV rated busbars [28]), an overall improvement in the time to reach the

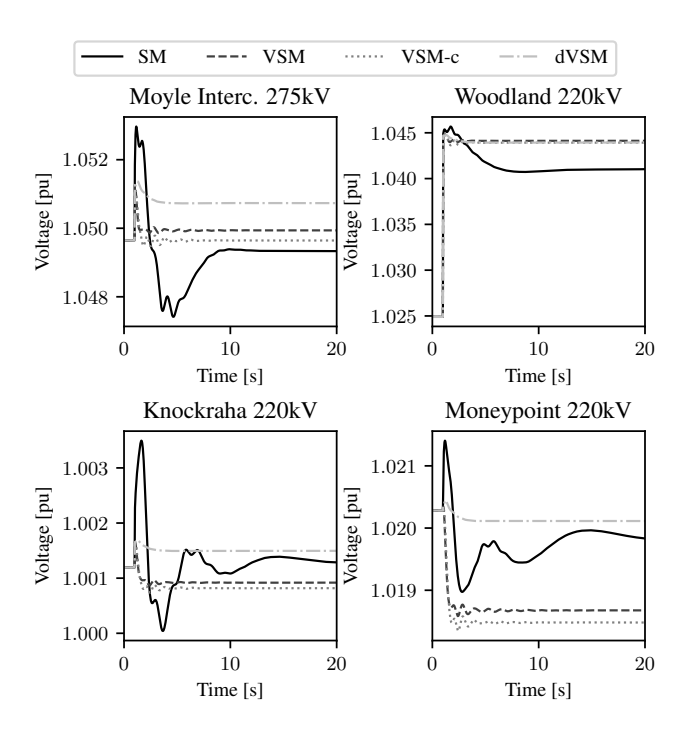


Fig. 10: Irish system - Voltage at representative buses after the loss of the East to West Interconnector 500 MW for different control setups of the GSC.

TABLE I: Irish system - Performance metric $\mu_{\rm ts}$ after the loss of the East to West Interconnector 500 MW for different control setups of the GSC

Metric	VSM	VSM Coupled	dVSM
$\mu_{\mathrm{t}, ho} \ \mu_{\mathrm{t},\omega} \ \mu_{\mathrm{t}}$	2.458×10^{-5}	4.006×10^{-5}	1.454×10^{-4}
	5.385×10^{-4}	5.365×10^{-4}	1.206×10^{-7}
	5.631×10^{-4}	5.765×10^{-4}	1.455×10^{-4}
$\mu_{\mathrm{s},\omega}$ $\mu_{\mathrm{s},v}$ μ_{s}	1.350×10^{-2}	1.350×10^{-2}	1.206×10^{-7}
	6.841×10^{-3}	6.372×10^{-3}	3.216×10^{-3}
	2.034×10^{-2}	1.987×10^{-2}	3.216×10^{-3}
$\mu_{ m ts}$	2.090×10^{-2}	2.045×10^{-2}	3.362×10^{-3}

steady state of the voltage across the buses of the system and the frequency of the CoI is observed. The interaction among PSS and AVR of the SMs is clearly observed in the voltage transient through all the buses of the system. This transient is mitigated due to the more homogeneous voltage and frequency control participation inherently provided by the GSC.

Table I presents the values of the metric described in Section II-A. This analysis evaluates the performance of three control strategies based on the GSC (VSM, VSM-c, and dVSM) following the loss of the 500 MW East-to-West Interconnector. The VSM-c configuration shows a slight improvement over the VSM by exploiting the inherent trade-off and coupling between frequency and voltage dynamics.

The dVSM demonstrates a significant improvement in overall dynamic performance. However, this performance gain is due to a fundamentally different power balancing mechanism compared to conventional strategies. Due to the inductive nature of the transmission grid, the dVSM has a local effect on the active power, which can sometimes be undesirable in systems with buses that have high voltage sensitivity and generators that lack significant power reserve.

Figure 11 shows the total active and reactive power provided by all generators with different GSC configurations in the upper panels, and the active and reactive power provided by the generators located at buses WHITEGAT and PBEGG4 in the lower panels. The total active power remains almost the same, but its distribution for the dVSM configuration is different from that of the VSM and the VSM-c. A similar effect occurs in the distribution of reactive power. However, the total reactive power is significantly different across the three schemes.

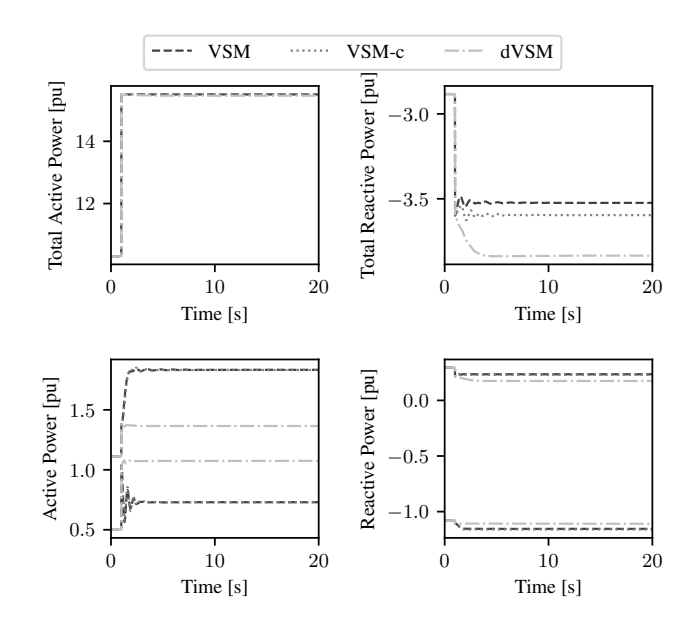


Fig. 11: Irish system - Total active and reactive power (in pu, upper panels) provided by all GSC-based generators, along with the active and reactive power provided by the generators located at buses WHITEGAT and PBEGG4 (lower panels), following the loss of the 500 MW East-to-West Interconnector for different GSC control setups.

IV. CONCLUSIONS

This paper proposes a novel control framework, namely Generalized Swing Control (GSC), which leverages the inherent flexibility of IBRs by extending the energy conversion principles of the swing equation to the complex domain. The mathematical properties of the GSC are analyzed within the QEP framework, with a focus on physical terms, namely inertia (M), damping (D), and stiffness (K).

Monte Carlo simulations are employed to enhance parameter tuning and assess the stability of GSC implementations. Several GSC configurations—including the VSM, extended VSM, coupled VSM, and dVSM—are evaluated using performance metrics such as the unstable simulation rate and the $\mu_{\rm ts}$ index (proposed to weight transient and steady-state variations). Tests are carried out based on the WSCC 9-bus system and a realistic-size model of the all-island Irish transmission system. Results demonstrate the framework's flexibility and its capability to enhance on power system stability. The GSC provides a unified approach to design GFM schemes, effectively enhancing system damping and inertial response.

The proposed framework, currently designed for a twodimensional vector space, can be extended to higherdimensional spaces. Therefore, future work will focus on utilizing the framework proposed in [29] to control the *geometric* frequency — a generalization of the CF and, consequently, of the conventional frequency. Additionally, sophisticated implementations of the different configurations of GSC, such as including current limiting, right-through modes, and parameter tuning, will be explored.

APPENDIX

The CF is a physical quantity that can also act as a derivative operator of any complex number with non-null magnitude [30]. For example, considering a complex time-dependent quantity, say \bar{u} , this can be written as:

$$\bar{u} = u \exp(j\alpha) = \exp(\ln u + j\alpha),$$
 (12)

where $u \neq 0$ and α are the magnitude and phase angle of \bar{u} , respectively. Assuming $\ln u$ and α are smooth functions of time, the time derivative of \bar{u} gives:

$$\bar{u}' = ((\ln u)' + \jmath \alpha') \exp(\ln u + \jmath \alpha)$$

$$= (u'/u + \jmath \alpha') \bar{u} = (\rho_u + \jmath \omega_u) \bar{u}$$

$$= \bar{n}_u \bar{u}.$$
(13)

The quantity $\bar{\eta}_u$ is the CF of \bar{u} , and ρ_u and ω_u are its real and imaginary parts, respectively.

REFERENCES

- [1] F. Milano, F. Dörfler, G. Hug, D. J. Hill, and G. Verbič, "Foundations and challenges of low-inertia systems," in *Power Systems Computation Conference (PSCC)*, 2018, pp. 1–25.
- [2] H. Cheng, C. Li, A. M. Y. M. Ghias, and F. Blaabjerg, "Dynamic coupling mechanism analysis between voltage and frequency in virtual synchronous generator system," *IEEE Trans. on Power Systems*, vol. 39, no. 1, pp. 2365–2368, 2024.
- [3] K. Su et al., "Fast frequency response analysis for grid- following and grid-forming controlled bess considering voltage coupling effect," *IEEE Trans. on Power Delivery*, vol. 40, no. 4, pp. 2412–2425, 2025.
- [4] Y. Laba, A. Bruyère, F. Colas, and X. Guillaud, "PQ decoupling on grid-forming converter connected to a distribution network," in *IEEE PEDG*, 2022, pp. 1–6.
- [5] W. Zhong, G. Tzounas, and F. Milano, "Improving the power system dynamic response through a combined voltage-frequency control of distributed energy resources," *IEEE Trans. on Power Systems*, vol. 37, no. 6, pp. 4375–4384, 2022.
- [6] R. Bernal and F. Milano, "Improving voltage and frequency control of ders through dynamic power compensation," *Electric Power Systems Research*, vol. 235, p. 110768, 2024.
- [7] —, "Complex frequency-based control for inverter-based resources," Journal of Modern Power Systems and Clean Energy, vol. 13, no. 5, pp. 1630–1641, 2025.
- [8] M. S. Toularoud, M. K. Rudposhti, S. Bagheri, and A. H. Salemi, "A hierarchical control approach to improve the voltage and frequency stability for hybrid microgrids-based distributed energy resources," *Energy Reports*, vol. 10, pp. 2693–2709, 2023.
- [9] W. Du, K. P. Schneider, G. P. Wiegand, F. K. Tuffner, J. Xie, and O. L. Dent, "A supplemental control for dynamic voltage restorers to improve the primary frequency response of microgrids," *IEEE Trans. on Smart Grid*, vol. 14, no. 2, pp. 878–888, 2023.
- [10] M. Lu, "Virtual oscillator grid-forming inverters: State of the art, modeling, and stability," *IEEE Trans. on Power Electronics*, vol. 37, no. 10, pp. 11 579–11 591, 2022.
- [11] M. Shadoul et al., "A comprehensive review on a virtual-synchronous generator: Topologies, control orders and techniques, energy storages, and applications," *Energies*, vol. 15, no. 22, 2022.

- [12] C. Collados-Rodríguez et al., "Stability analysis of systems with high vsc penetration: Where is the limit?" *IEEE Trans. on Power Delivery*, vol. 35, no. 4, pp. 2021–2031, 2020.
- [13] D. Ramasubramanian and E. Farantatos, "Viability of synchronous reference frame phase locked loop inverter control in an all inverter grid," in *IEEE PES General Meeting (PESGM)*, 2020, pp. 1–5.
- [14] R. Bernal and F. Milano, "Transient slack capability," 2025. [Online]. Available: https://arxiv.org/abs/2505.17984
- [15] Q.-H. Wu et al., "Transient stability analysis of large-scale power systems: A survey," CSEE Journal of Power and Energy Systems, vol. 9, no. 4, pp. 1284–1300, 2023.
- [16] Y. Sun, J. Ma, J. Kurths, and M. Zhan, "Equal-area criterion in power systems revisited," *Proceedings of the Royal Society A: Mathematical*, *Physical and Engineering Sciences*, vol. 474, p. 20170733, 2018.
- [17] B. Fan and X. Wang, "A Lyapunov-based nonlinear power control algorithm for grid-connected VSCs," *IEEE Trans. on Industrial Electronics*, vol. 69, no. 3, pp. 2916–2926, 2022.
- [18] S. Zhang, Z. Zhu, and Y. Li, "A critical review of data-driven transient stability assessment of power systems: Principles, prospects and challenges," *Energies*, vol. 14, no. 21, 2021.
- [19] C. Feng, L. Huang, X. He, Y. Wang, F. Dorfler, and C. Kang, "Hybrid oscillation damping and inertia management for distributed energy resources," *IEEE Trans. on Power Systems*, pp. 1–16, 2025.
- [20] Y. Yu, Y. Guan, W. Kang, J. C. Vasquez, and J. M. Guerrero, "A generic inertial-response preserved active-damping control for gridforming inverters emulating synchronous machines," *IEEE Trans. on Industrial Electronics*, vol. 72, no. 6, pp. 5897–5905, 2025.
- [21] R. Ma, J. Li, J. Kurths, S. Cheng, and M. Zhan, "Generalized swing equation and transient synchronous stability with pll-based vsc," *IEEE Trans. on Energy Conversion*, vol. 37, no. 2, pp. 1428–1441, 2022.
- [22] F. Tisseur and K. Meerbergen, "The quadratic eigenvalue problem," SIAM Review, vol. 43, no. 2, pp. 235–286, 2001.
- [23] P. Sauer and M. Pai, Power system dynamics and stability. Prentice Hall, 1998.
- [24] M. Adeen et al., "On the calculation of the variance of algebraic variables in power system dynamic models with stochastic processes," *IEEE Trans. on Power Systems*, vol. 38, no. 2, pp. 1739–1742, 2023.
- [25] F. Milano, "A Python-based software tool for power system analysis," in *IEEE PES General Meeting*, 2013, pp. 1–5.
- [26] ——, "Dual grid-forming converter," *IEEE Trans. on Power Systems*, vol. 40, no. 2, pp. 1993–1996, 2025.
- [27] B. Tan et al., "Power system inertia estimation: Review of methods and the impacts of converter-interfaced generations," Int. J. of Electrical Power & Energy Systems, vol. 134, p. 107362, 2022.
- [28] EirGrid, Grid Code Version 15, Jul. 23 2025, issue Date: 23 July 2025, 463 pages.
- [29] F. Milano, "A geometrical interpretation of frequency," *IEEE Trans. on Power Systems*, vol. 37, no. 1, pp. 816–819, 2022.
- [30] —, "Complex frequency," *IEEE Trans. on Power Systems*, vol. 37, no. 2, pp. 1230–1240, 2022.